SUPPLEMENTARY INFORMATION

Nano-Engineered Ag@MgO-Embedded Chitosan Hydrogel Patch for Potent Antibacterial, Antibiofilm, and Infected Wound Healing

Surbhi Sharma[1 #], Anjali Upadhyay[2 #], Durba Banerjee[2], Alok Kumar[3], Pralay Maiti[3], Chandra Shekhar Pati Tripathi[4], Sudip Mukherjee[* 2], and Debanjan Guin[* 1]

[1]*Department of Chemistry, Institute of Science, Banaras Hindu University, Varanasi-221005*

[2]*School of Biomedical Engineering at Indian Institute of Technology, Banaras Hindu University, Varanasi 221005*

[3]*School of Materials Science and Technology, Indian Institute of Technology, Banaras Hindu University, Varanasi 221005*

[4]*Department of Physics, Institute of Science, Banaras Hindu University, Varanasi-221005*

S.I.1 Materials

Sucrose ($C_{12}H_{22}O_{11,}$ CAS No. 57-50-1, purity ≥ 99%) was obtained from Fisher Scientific, while the compound Magnesium nitrate ($MgNO_3.6H_2O$, CAS No.13446-18-9, purity ≥ 99%), silver nitrate ($AgNO_3$, CAS No. 7761-88-8, purity ≥ 99.5%,) and trisodium citrate dihydrate (CAS No. 6132-04-3, purity ≥ 99%,) were acquired from Merck Life Science Pvt. Ltd. Chitosan (low molecular weight, CAS No. 9012-76-4, the degree of deacetylation is ≥ 75%), 2′,7′-dichlorodihydrofluorescein diacetate (DCFHDA, CAS No.4091-99-0, purity ≥97%). were purchased from Sigma-Aldrich. LB broth and nutrient agar were purchased from HiMedia Laboratories Pvt (CAS No. M1245-500G and M001500G), purity ≥ 97%). Ltd. 4′,6-Diamidino-2-phenylindole (DAPI) (CAS No.28718-90-3, purity ≥ 95%), propidium iodide (PI) (CAS No.25535-16-4, purity ≥ 95%), 2,2-diphenyl-1-picrylhydrazyl (DPPH) (CAS No. 1898-66-4, purity ≥ 98%) DMSO (CAS No. 67-68-5, purity ≥ 99%), PBS, and glutaraldehyde (CAS No. 111-30-8, purity ≥ 99%) were obtained from SRL (Sisco Research Laboratories Pvt. Ltd.) - India. GFP-tagged *E. coli* was a generous gift from Prof. Bama Charan Mondal, BHU, Varanasi, and *B. subtilis* was a generous gift from Prof. Avnish Parmar, IIT BHU, and *S. aureus* was obtained by IMS (Institute of Medical Sciences) BHU. All chemicals were used as received without further purification. Ultrapure distilled water (D.W.) was consistently utilized throughout all the experiments.

S.I.2 Instrumentation

Crystal structures were analyzed using the Bruker Model D8 Advance (Eco) instrument for X-ray diffraction (XRD). To delve into the chemical composition and

states of the Ag@MgO-NSs nanocomposite and Ag@MgO/PVDF dip catalyst, X-ray photoelectron spectroscopy (XPS) with the PHI 5000 Versa Probe III spectrometer from ULVAC-PHI, Inc., was utilized. For a detailed exploration of the morphological features of the nanocomposite, transmission electron microscopy (TEM) was employed with the FEI TECNAI 20 G2 20 instrument. The CARL ZEISS Model EVO-18 scanning electron microscope facilitated a comprehensive study of the synthesized morphologies of the hydrogels. Rheological measurements of control-H and Cs-AMO were characterized using a strain-controlled Rheometer (MCR702, Anton Paar) equipped with parallel plate geometry (1 mm gap, 25 mm diameter). A dynamic strain sweep was performed at room temperature with a constant frequency of 5 rad s^{-1}. Strain was varied from 0.01 to 1500%, and the storage modulus (G′) and loss modulus (G″) were measured to identify the linear viscoelastic region (LVER) where the modulus remains unaffected by a change in strain amplitude. Using this strain-sweep test, the suggested LVER strain is 1%.

Frequency sweep test: Within the LVER (1.0% strain), a frequency sweep was conducted for control-H and Cs-AMO hydrogel at room temperature (27°C) across a range of angular frequencies (ω) from 100 to 0.1 rad s^{-1}. Various viscoelastic factors, including the storage modulus (G'), loss modulus (G''), and complex viscosity(η^*), were measured.

The release profile of Ag^+ ions was quantitatively analyzed using Inductively Coupled Plasma Mass Spectrometry (ICP-MS) on an Agilent 7800 ICP-MS system.

S.I.3 Characterization studies

The crystalline structure of the synthesized MgO nanosheets (MgO-NSs) and the Ag@MgO-NSs nanocomposite was examined using X-ray diffraction (XRD). As shown in Figure S1(a), the calcined MgO-NSs exhibit sharp and well-resolved diffraction peaks, indicating their high crystallinity. The diffraction reflections observed at 2θ values of 36.8°, 42.8°, 62.3°, 74.6°, and 78.6° can be indexed to the (111), (200), (220), (311), and (222) crystallographic planes of face-centered cubic (FCC) MgO, in good agreement with the standard JCPDS card (No. 45–0946)[1]. The absence of any additional diffraction peaks confirms the phase purity of the prepared MgO-NSs.

For the Ag@MgO-NSs nanocomposite, the XRD pattern displays all the characteristic peaks of MgO along with an additional diffraction peak at 38.8°, which corresponds to the (111) plane of FCC silver (JCPDS card No. 04-0783)[2]. The appearance of this peak confirms the successful decoration of Ag nanoparticles onto the MgO nanosheets, while the unchanged MgO diffraction pattern suggests that the crystal structure of MgO remains intact after Ag incorporation[3].

The TEM micrographs shown in Figure S1(b) confirm the characteristic nanosheet structure of the Ag@MgO composite. Distinct dark nanodots are uniformly dispersed over the MgO nanosheet surface, providing clear evidence of successful silver nanoparticle decoration and homogeneous distribution across the support.

The UV-visible absorption spectrum of the AgNPs (Figure S1(d)) shows a clear absorption peak centered at around 400 nm. This characteristic peak is attributed to the surface plasmon resonance (SPR) of AgNPs, which belongs to the π–π* transition.

Fourier-transform infrared (FT-IR) spectroscopy was employed to analyze the bonding characteristics of the synthesized MgO nanosheets and the Ag@MgO nanocomposite. As presented in Figure S1(c), the spectrum of Ag@MgO-NSs shows a decreased intensity of the band around 475 cm^{-1}, which is associated with Mg-O vibrations, suggesting surface modification following silver deposition. A broad absorption band centered at approximately 3443 cm^{-1} is attributed to O-H stretching vibrations, likely arising from surface hydroxyl groups or adsorbed moisture. The band observed near 1462 cm^{-1} can be assigned to C=O stretching vibrations, while the feature around 1637 cm^{-1} corresponds to asymmetric stretching of carbonyl-related groups. These spectral changes collectively support the successful formation of the Ag-decorated MgO nanosheet composite.[3, 4]

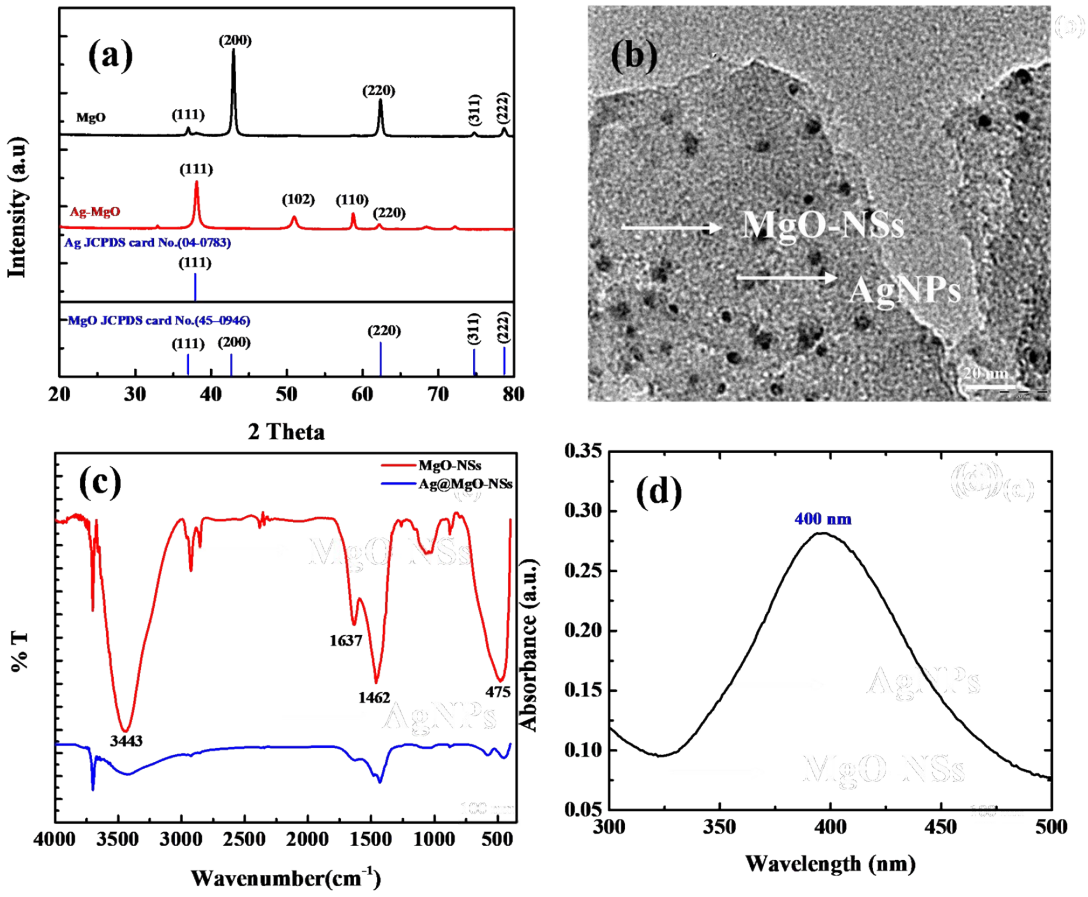

Figure S1 (a) XRD spectra of MgO-NSs and Ag@MgO-NSs nanocomposite powder (b) and (c) FT-IR spectra of MgO-NSs and Ag@MgO-NSs (d) UV-Vis spectra of AgNPs .

X-ray photoelectron spectroscopy (XPS) was performed to investigate the surface composition and chemical states of the Ag@MgO nanosheets. The survey spectrum (Figure S2(a)) exhibits distinct signals corresponding to Mg, O, and Ag, along with a carbon peak arising from surface adventitious carbon, confirming the successful formation and chemical purity of the nanocomposite. The high-resolution Ag 3d spectrum (Figure S2(b)) shows two characteristic peaks located at binding energies of 365.45 eV and 371.53 eV, which are assigned to Ag $3d_{5/2}$ and Ag $3d_3/_2$, respectively. The observed spin-orbit splitting of approximately 6 eV is consistent with metallic silver (Ag^0), indicating that silver is present predominantly in its reduced state rather than as oxidized species.

The O 1s spectrum (Figure S2(c)) can be deconvoluted into two components. The peak centered at 529.4 eV is attributed to lattice oxygen (O^{2-}) in MgO, while the second contribution at 528.4 eV is associated with oxygen species influenced by the presence of silver at the surface. Furthermore, the Mg 1s spectrum (Figure S2(d)) displays peaks at 1300.4 eV and 1301.4 eV, confirming the presence of magnesium in its characteristic +2 oxidation state.[3, 5-9]

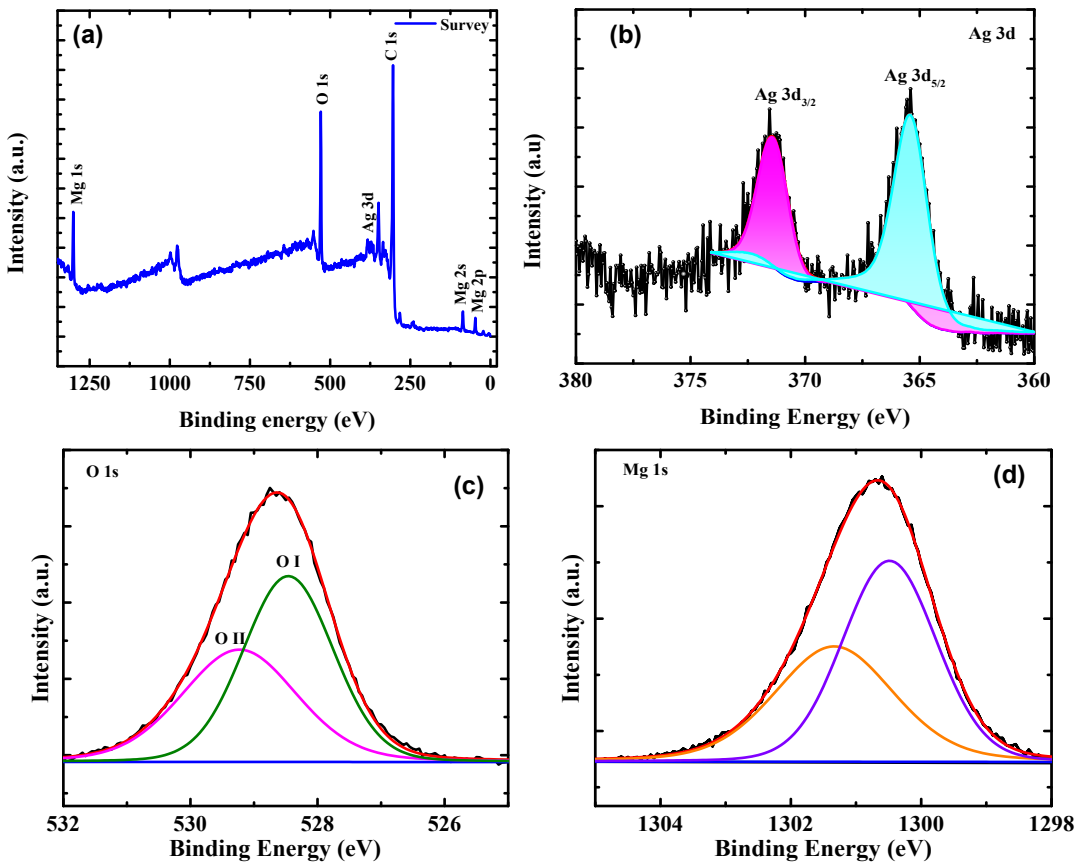

Figure S2 XPS plot of (a) survey (b) Ag 3d (c) deconvoluted O 1s (d) deconvoluted Mg 1s

S.I.4 Swelling Behaviour of Hydrogel

The swelling behavior of Cs-AMO and control-H hydrogels was evaluated using the following procedure. Initially, each hydrogel sample was immersed in a sealed tube filled with PBS (pH 7) at room temperature. At predetermined time intervals, the hydrogels were taken out, gently blotted with filter paper to remove excess surface moisture, and weighed. This process was continued repeatedly until no further change in hydrogel weight was observed. The swelling ratio was then calculated based on the measured mass values. Each experiment was carried out four times for every sample, and the final result was reported as the average value.

The swelling ratio (SR) was calculated using the equation:

$$SR = (W_t - W_0) / W_0 \times 100\ \%$$

where SR represents the swelling ratio, W_t denotes the mass of the hydrogel at a specific time, and W_0 corresponds to the initial mass of the hydrogel.[10]

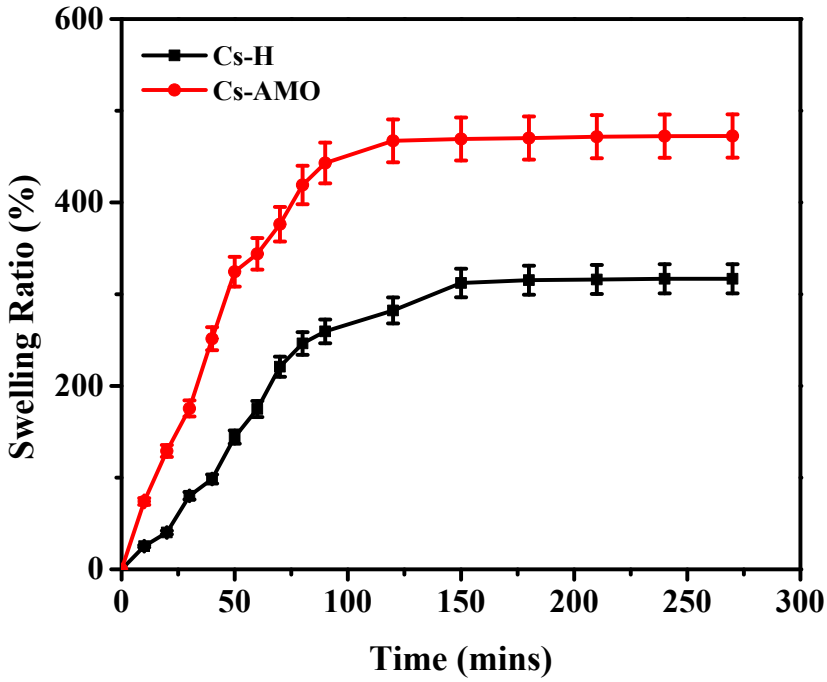

Figure S3. Swelling behavior of Cs-H, Cs-AMO hydrogels.

S.I.5 Degradation Behaviour of Cs-AMO Hydrogel

The degradation behavior of the Cs-AMO hydrogel was evaluated in PBS over a period of 9 days by monitoring the change in sample weight. The hydrogel retained approximately 77% of its initial weight after 5 days and about 41% after 9 days, indicating gradual and controlled degradation while maintaining structural integrity during the study period. Visual observations further confirmed the slow and sustained degradation behavior of the patch throughout the incubation duration.

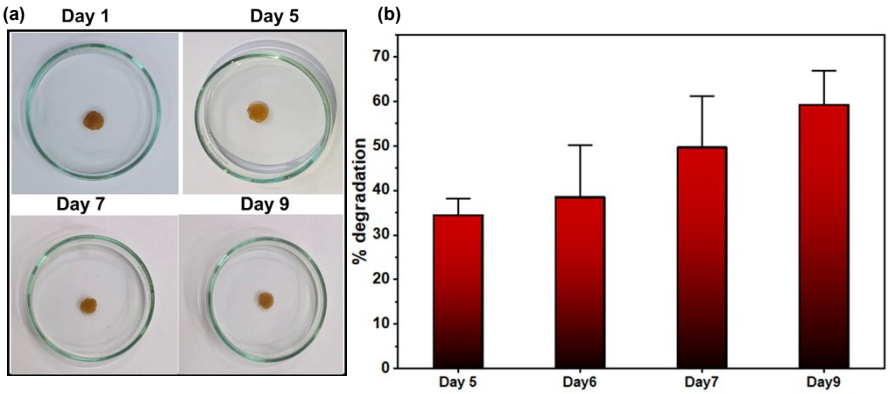

Figure S4. Degradation images of Cs-AMO hydrogel until day 9 in PBS (b) degradation plot of Cs-AMO hydrogel by measuring the weight at different time scales.

S.I.6 Release Behavior of Silver Ions

The release kinetics of silver ions from the Cs-AMO hydrogel was systematically evaluated to understand its sustained antibacterial potential. The silver ion release study was carried out by incubating the hydrogel samples in phosphate-buffered saline (PBS) at room temperature, with all experiments performed in triplicate (n = 3). The release behavior was monitored at predetermined time intervals on days 1, 2, and 3, and the reported release value corresponds to each day of incubation. The results revealed that at day 1, day 2, and day 3 (2.1 µg, 6 µg, and 18 µg, respectively), Ag release was observed (as determined by ICP-MS) over the study period, indicating sustained release of silver from the hydrogel matrix. The release profile suggests that the chitosan network enables controlled diffusion of silver ions rather than an immediate burst release, which is advantageous for maintaining prolonged antimicrobial activity and effective wound healing while minimizing potential cytotoxic effects. Such sustained ion release is particularly important in chronic wound environments, where persistent bacterial presence requires continuous antimicrobial action. The observed release behavior supports the hydrogel's ability to provide long-term antibacterial protection, thereby contributing to effective infection control and enhanced wound healing outcomes.

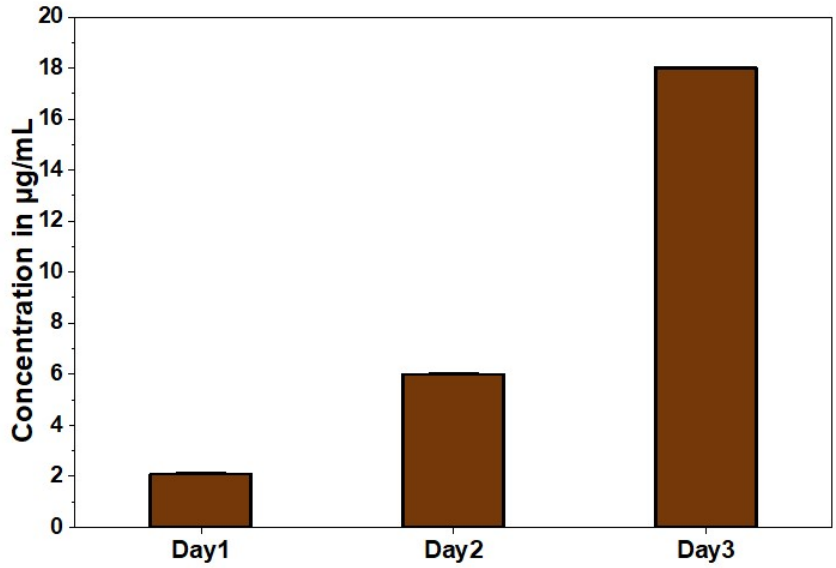

Figure S5. The release behavior of silver ions at predetermined time intervals on days 1, 2, and 3

S.I.7 Comparative study of literature reported various commercial metal oxide nanocomposites.

Table S1. A comparative study of literature reported various commercial metal oxide nanocomposites.

System	Advantages	Limitations
Ag NPs	Silver shows strong broad-spectrum antibacterial activity and is widely used in wound dressings due to effective Ag^+ ion release that reduces bacterial load.[11]	Aggregation, burst ion release, discoloration, and dose-dependent cytotoxicity remain major concerns, immobilization/support materials are often needed to reduce leaching and improve control. [12]
ZnO NPs	ZnO offers effective antibacterial activity via Zn^{2+} release and supports epithelial repair, with many ZnO-based hydrogels showing benefits in infected wound healing[13]	Antibacterial mechanism is not fully consistent across studies, performance depends on formulation, and high ZnO loading may increase toxicity or impair fibroblast migration/tissue repair.[14]
TiO_2 NPs	Chemically stable, generally biocompatible, and widely explored for antibacterial coatings and wound materials, TiO_2-containing dressings have shown improved regeneration in some studies[15]	A key limitation is that TiO_2 often shows weak visible-light activity and may depend on photoactivation for stronger ROS-mediated antimicrobial action, which can limit practical wound use under dark physiological conditions[15]
Cu/CuO NPs	Strong antibacterial action and potential pro-angiogenic/pro-regenerative roles related to copper, copper-containing hydrogels have shown promise in infected wound healing.[16]	Copper systems can face oxidation instability and a narrower safety window because excess Cu can enhance oxidative stress and cytotoxicity.[17]
ZnO/TiO_2 composites	The heterojunction concept can improve ROS generation and antibacterial behavior compared with single oxides. ZnO/TiO_2 combinations are frequently proposed as efficient antimicrobial composites[18]	ZnO/TiO_2 systems may exhibit light-dependent antibacterial activity, potential cytotoxicity at higher concentrations, and comparatively limited direct wound-healing validation[18]
CuO/TiO_2 composites	Reported to show enhanced antibacterial performance and useful surface functionality; emerging studies suggest biological potential[19]	Direct wound-dressing evidence remains comparatively limited, and the system may still inherit both TiO_2 light-dependence and Cu-associated toxicity concerns[19]
ZnO/CuO composites	Strong antibacterial activity against skin pathogens, including MDR organisms, has been reported. Porous chitosan-supported ZnO/CuO systems also show good biocompatibility in some studies[20]	Potential cumulative metal-ion toxicity remains a concern, and not all studies include full wound-healing validation or long-term biosafety analysis[21]
Ag/MgO or	Ag@MgO systems offer strong	Still less explored than Ag-only or

Ag@MgO-type systems	synergistic antibacterial and antibiofilm activity with improved stability and controlled Ag^+ release[22]	ZnO-based wound systems, so more mechanistic and translational studies are needed[23]

References

1. Priyadarsini, G.; Pravitha, S.; Deepa, J., Structural integrity and optical properties of MgO nanoparticles synthesized via solution combustion. *Next Nanotechnology* **2026,** *9*, 100429.
2. Ali, M. H.; Azad, M. A. K.; Khan, K.; Rahman, M. O.; Chakma, U.; Kumer, A., Analysis of crystallographic structures and properties of silver nanoparticles synthesized using PKL extract and nanoscale characterization techniques. *ACS omega* **2023,** *8* (31), 28133-28142.
3. Sharma, S.; Sharma, K.; Majhi, S.; Tripathi, C. S. P.; Guin, D., Facile synthesis of Ag NPs@ MgO nanosheets for quantitative SERS-based detection and removal of hazardous organic pollutants. *Spectrochimica Acta Part A: Molecular and Biomolecular Spectroscopy* **2024,** *323*, 124885.
4. Sharma, S.; Sharma, K.; Kumar, A.; Tripathi, C. S. P.; Guin, D., Fabrication of a non-enzymatic electrochemical sensor based on magnesium oxide nanosheets for selective and sensitive detection of hydrogen peroxide in food samples. *Journal of Applied Electrochemistry* **2024,** *54* (6), 1365-1377.
5. Shkir, M.; AlAbdulaal, T.; Manthrammel, M. A.; Khan, F. S., Novel MgO and Ag/MgO nanoparticles green-synthesis for antibacterial and photocatalytic applications: A kinetics-mechanism & recyclability. *Journal of Photochemistry and Photobiology A: Chemistry* **2024,** *449*, 115398.
6. Peterka, D.; Tegenkamp, C.; Schröder, K.-M.; Ernst, W.; Pfnür, H., Oxygen surplus and oxygen vacancies on the surface of epitaxial MgO layers grown on Ag (100). *Surface science* **1999,** *431* (1-3), 146-155.
7. Umaralikhan, L.; Jamal Mohamed Jaffar, M., Green synthesis of MgO nanoparticles and it antibacterial activity. *Iranian Journal of Science and Technology, Transactions A: Science* **2018,** *42*, 477-485.
8. Güney, H.; İskenderoğlu, D., The effect of Ag dopant on MgO nanocrystallites grown by SILAR method. *Materials Science in Semiconductor Processing* **2018,** *84*, 151-156.
9. Alaizeri, Z. M.; Alhadlaq, H. A.; Aldawood, S.; Akhtar, M. J.; Amer, M. S.; Ahamed, M., Facile synthesis, characterization, photocatalytic activity, and cytotoxicity of Ag-doped MgO nanoparticles. *Nanomaterials* **2021,** *11* (11), 2915.
10. Li, M.; Liang, Y.; He, J.; Zhang, H.; Guo, B., Two-pronged strategy of biomechanically active and biochemically multifunctional hydrogel wound dressing to accelerate wound closure and wound healing. *Chemistry of Materials* **2020,** *32* (23), 9937-9953.
11. Dai, Q.; Jia, R.; Li, H.; Yang, J.; Qin, Z., Preparation and application of sustained-release antibacterial alginate hydrogels by loading plant-mediated silver nanoparticles. *ACS Sustainable Chemistry & Engineering* **2024,** *12* (4), 1388-1404.
12. Albao, M. J. F.; Calsis, J. R. F.; Dancel, J. O.; De Juan-Corpuz, L. M.; Corpuz, R. D., Silver nanoparticle-infused hydrogels for biomedical applications: a comprehensive review. *Journal of the Chinese Chemical Society* **2025,** *72* (2), 124-162.
13. Liu, H.; Yang, Y.; Deng, L.; Shen, Z.; Huang, Q.; Shah, N. G.; Chen, W.; Zhang, Y.; Wang, X.; Yu, L., Antibacterial and antioxidative hydrogel dressings based on tannic acid-gelatin/oxidized sodium alginate loaded with zinc oxide nanoparticles for promoting wound healing. *International Journal of Biological Macromolecules* **2024,** *279*, 135177.
14. Pino, P.; Bosco, F.; Mollea, C.; Onida, B., Antimicrobial nano-zinc oxide biocomposites for wound healing applications: a review. *Pharmaceutics* **2023,** *15* (3), 970.
15. Lu, B.; Zhang, J.; Zhu, G.; Liu, T.; Chen, J.; Liang, X., Highly hydrophilic and dispersed TiO2 nano-system with enhanced photocatalytic antibacterial activities and accelerated tissue regeneration under visible light. *Journal of Nanobiotechnology* **2023,** *21* (1), 491.

16. Sandoval, C.; Rios, G.; Sepulveda, N.; Salvo, J.; Souza-Mello, V.; Farias, J., Effectiveness of copper nanoparticles in wound healing process using in vivo and in vitro studies: A systematic review. *Pharmaceutics* **2022,** *14* (9), 1838.
17. Gudkov, S. V.; Burmistrov, D. E.; Fomina, P. A.; Validov, S. Z.; Kozlov, V. A., Antibacterial properties of copper oxide nanoparticles. *International Journal of Molecular Sciences* **2024,** *25* (21), 11563.
18. Menazea, A.; Awwad, N. S., Antibacterial activity of TiO2 doped ZnO composite synthesized via laser ablation route for antimicrobial application. *Journal of Materials Research and Technology* **2020,** *9* (4), 9434-9441.
19. Rajkumar, M.; Presley, S. D.; Begum, M. Y.; Alamri, A.; Al Fatease, A.; Girigoswami, K.; Govindaraj, P.; Sampath, S.; Madhan, R.; Deepak, P., Biogenic Synthesis of CuO-TiO2 Nanocomposites from Senna auriculata (L.) Roxb. Plant Extract and its Evaluation of Antioxidant, Antibacterial and Anticancer Activity of HepG2 Cell lines. *Biocatalysis and Agricultural Biotechnology* **2025**, 103787.
20. Govindasamy, G. A.; Mydin, R. B. S.; Sreekantan, S.; Harun, N. H., Compositions and antimicrobial properties of binary ZnO–CuO nanocomposites encapsulated calcium and carbon from Calotropis gigantea targeted for skin pathogens. *Scientific reports* **2021,** *11* (1), 99.
21. Takele, E.; Feyisa Bogale, R.; Shumi, G.; Kenasa, G., Green synthesis, characterization, and antibacterial activity of CuO/ZnO nanocomposite using Zingiber officinale rhizome extract. *Journal of Chemistry* **2023,** *2023* (1), 3481389.
22. Saravanakumar, K.; Sathiyaseelan, A.; Zhang, X.; Choi, M.; Wang, M.-H., Bimetallic (Ag and MgO) nanoparticles, Aloe vera extracts loaded xanthan gum nanocomposite for enhanced antibacterial and in-vitro wound healing activity. *International Journal of Biological Macromolecules* **2023,** *242*, 124813.
23. Dam, P.; Celik, M.; Ustun, M.; Saha, S.; Saha, C.; Kacar, E. A.; Kugu, S.; Karagulle, E. N.; Tasoglu, S.; Buyukserin, F., Wound healing strategies based on nanoparticles incorporated in hydrogel wound patches. *RSC advances* **2023,** *13* (31), 21345-21364.